Segmental flexibility of bispecific T-cell engagers regulates the dynamics of immune synapse formation

Author list: Oskar Staufer[1], Alexander Leithner[1], Sally Zhou[2], Maureen Crames[2], Stephen Comeau[2], David Young[2], Sarah Low[2], Edward Jenkins[3,4], Simon J. Davis[3,4], Andrew Nixon[2], Noah Pefaur[2], Srinath Kasturirangan[2], Michael L. Dustin[1,*]

*Corresponding author: michael.dustin@kennedy.ox.ac.uk

Affiliations:

1: The Kennedy Institute of Rheumatology, University of Oxford, OX3 7FY Oxford, United Kingdom

2: Biotherapeutics Discovery, Boehringer Ingelheim, Ridgefield, CT, 06877, USA

3: Medical Research Council Human Immunology Unit, University of Oxford, OX3 9DU Oxford, United Kingdom

4: Radcliffe Department of Medicine, The University of Oxford, OX3 9DU Oxford, United Kingdom

Classification: Biological Science, Immunology and Inflammation

Keywords: Immunological synapse, breast cancer, supported lipid bilayers, immunotherapy

Abstract

Bispecific T-cell engagers (TcEs) are antibody-based immunotherapeutic drugs that specifically direct lymphocyte effector functions against tumors. TcEs have one arm with affinity for an activating immunoreceptor connected through a flexible hinge to a distinct arm with affinity for a tumor antigen to achieve tumor killing by cytotoxic immune cells. Understanding the structure-function relationships between TcE architecture, immunological synapse formation and function could accelerate design of new TcE-based cancer therapies. Here, we engineer and systematically characterize TcE formats with antigen binding antibody fragments or single chain variable fragments linked together in *cis* through immunoglobulin G1 hinge or in *trans* across the antibody constant fragment. The TcEs were tested in $CD8^+$ T-cell killing of $Her2^+$ breast cancer cells and evaluated by high-content imaging of immunological synapse formation on a supported lipid bilayer (SLB) platform. We find that *cis* TcEs perform better than a *trans* TcE for T-cell mediated killing. Quantification of synapse formation dynamics revealed that all three *cis* TcEs tested, created close contacts of < 16 nm leading to rapid synapse formation and integrin activation. In contrast, the *trans* TcE formed close contacts averaging ≥ 16 nm and formed synapses more slowly with weaker integrin activation. We conclude that segmental flexibility is important for TcE function, but adding additional degrees of freedom through *trans* formats has a cost for killing efficiency that may be explained by failure of close contact formation and integrin activation.

Introduction

The past decade has witnessed a transition from systemic drugs that target tumors broadly, towards immunotherapies that specifically modulate immune responses against cancerous cells. Checkpoint inhibitors, that block inhibitory immune signaling, and genetically engineered T-cells, that express artificial T-cell receptors for targeted cancer cell killing, have joined the conventional arsenal of surgical resection, chemotherapy, and irradiation(1). Additionally, bispecific TcEs based on antibody scaffolds that are able to simultaneously bind to antigens on cancer and T-cells, have gained significant clinical interest as they represent a versatile, highly-potent and economical immunotherapeutic tool(2). TcEs are antibody-derived molecules harboring at least one arm that binds to an activating immunoreceptor such as the T-cell receptor (TCR) complex, and one arm directed against a tumor associated antigen (TAA). A plethora of TcE designs have been developed (3) that can be subcategorized into those retaining the Fc-region of IgGs and those that only feature antigen binding fragments (Fab) or smaller single chain variable fragment (scFv). While the smallest TcE consisting of two scFv and a short linker show improved penetration of solid tumors, constant fragment (Fc)-containing TcEs feature improved pharmacokinetic characteristics, such as extended circulation half-life, and better chemistry, manufacturing and controls (CMC) drug quality. One of the simplest TcE is based on using knob-in-hole engineering of Fab and Fc to generate an IgG-like molecule with arms binding different targets linked in *cis* across a single flexible hinge. Engineering can be simplified by replacing one or both Fab with a scFv. Within these Fc containing TcEs, variants have also been generated where scFv are attached in novel locations, such as in *trans* at the C-terminus of the Fc(3). Such a trans TcE has additional degrees for freedom with two flexible hinges at either end of the rigid Fc spacer.

Mechanistically, TcEs physically link polyclonal effector T-cells with cancer cells to promote the formation of cytolytic immune synapses (IS), exploiting the intrinsic cytotoxic machinery of T-cells for a therapeutic benefit(4) (**Figure 1A**). Since the first-in-class approval of blinatumomab in 2015, a multitude of different TcEs formats were (pre-)clinically assessed in solid and hematological tumors, particularly for lymphoblastic leukemia and Her2^{+} solid tumors. These assessments revealed significant variations in TcE efficacy and safety(2, 5). Extensive research efforts established that the pharmacodynamics and kinetics of TcEs are modulated by a variety of factors such as binding arm length, linker design, binding valency, Fc-engineering and binding arm positioning (*cis* and *trans*) (5, 6). However, the exact mechanism by which TcE architecture regulates the formation of IS and thus TcE potency, remains largely unexplored.

Synapse formation between T- and target cells is a highly orchestrated process dominated by a complex interplay of molecular self-assembly events and active cellular rearrangements. IS structure, maturation and signaling have been reviewed in detail elsewhere(7). Of note, central structural elements underlaying antigen recognition and signal integration in the IS include a TCR-enriched and F-actin depleted central supramolecular activation cluster (cSMAC), LFA1/ICAM-1-based peripheral adhesion sites (pSMAC) and a distal (dSMAC) region that is a site of F-actin polymerization and generation of signaling microclusters(8). The TCR is a complex multisubunit protein that may be impacted through TcEs by allostery(9), mechanotransduction, clustering(10-12) and large phosphatase exclusion from close contacts (13). Different TcE architectures may have a profound impact on proximity between the two cellular membranes presenting the TCR and TAA epitopes, which governs the exclusion of the large CD45 phosphatase (core ectodomain length = 16

nm(14)), from the TCR microclusters(15). This in turn, leads to locally increased phosphorylation of TCRs bound to peptide-major histocompatibility complexes as well as a supply of active Lck maintained by adjacent areas with CD45 and promotes downstream signaling and T-cell activation(13). TcEs targeting membrane distal epitopes on large TAAs show reduced cytotoxic potency (16, 17), which is predicted by phosphatase exclusion models. However, the segmented nature of TcEs, in contrast to the linear complex formed by TCR and pMHC, makes prediction about how TcE architecture will impact IS formation challenging. While the last decades of extensive research on IS formation have brought a detailed understanding of their maturation and signaling, the mechanism of IS formation mediated by TcEs has only been addressed by a small number of studies(4-6, 17-19). However, none of these studies has investigated the TcE structure-function relationship with respect to immunological synapse formation or two of its major steps- close contact formation and integrin activation. Consequently, several questions of fundamental relevance for TcE-based therapeutics remain(4): To what degree is canonical IS organization maintained by TcEs? How does TcE design alter the quality, quantity and duration of IS signaling? And does TcE architecture influence IS formation dynamics?

To study the effects of TcEs on formation of IS, we combined functional cell-based assays with a reductionistic supported lipid bilayer (SLB) systems. The latter allowed us to generate IS between T-cells and cancer cell-mimicking lipid membranes through additions of TcEs. SLBs have been established as effective surrogates of antigen-presenting cells (APC) that allow for imaging and quantitative description of the dynamics underpinning the molecular patterning processes during IS formation(20). Initial clinical trials produced promising results for TcE therapies targeting Her2^{+} breast cancer tumors, wherefore we focused our study on Her2/CD3

binding TcEs. This enabled us to compare IS formation triggered by TcEs of different architecture in a fully controlled and optically accessible setup; and to extract quantitative parameters of the IS (co-)signaling components. Our results suggest that TcE exert powerful control over close contact formation by T-cells as assessed by local CD45 density. We find that TcE in the *cis* configuration, with a single hinge connecting the binding arms, triggered efficient killing and CD45 exclusion whereas a TcE in the *trans* configuration, with a ~8 nm insert between two flexible hinges, was less efficient at triggering killing and didn't exclude CD45 despite being of similar overall dimensions to the largest *cis* format. Thus, while the trans format extents the potential number of interactions for a TcE, it is not functionally equivalent to the more biomimetic cis configuration.

Results

Functional analysis of TcE-mediated cytotoxicity

We began our study by designing several formats of IgG based bispecific TcEs with varying arm length in *cis* or *trans* configurations (**Figure 1B**). TcEs were engineered by knob-into-hole technology for monovalent binding with human Her2 through a membrane proximal epitope ~2 nm from the target surface and CD3ε about 4 nm from the T cell surface(21). The characteristic spacing generated by TCR-pMHC complexes between the T cell and target cell membrane is ~14 nm (22, 23). We hypothesized that an effective TcE will recapitulate this spacing in close contacts between the T cell and target. Previous structural and functional studies have highlighted the importance of the flexible hinge region for the antigen search range and IgG-based cancer therapy(24-26). Moreover, the linkers between antibody fragments have been shown

to act as entropic springs that dynamically adjust paratope spacing during antibody binding to antigens(27), a characteristic that is of special importance for membrane-confined reactions(28). These studies suggest that 10 pN force applied to IgG results in approximately 1 nm displacement, which is in the force range generated by actin at the IS interface on a single TCR level(29). Therefore, we included *cis* TcE Formats A-C with paratope spacings that bracket this range taking into account segmental flexibility (**Figure 1B**). We also include a *trans* Format D that has additional degrees of freedom with two hinges separated by the Fc domain. All TcEs were characterized by size exclusion chromatography (**Figure S1A,E**), hydrophobic interaction chromatography (**Figure S1B**), differential scanning calorimetry (**Figure S1C**) and biolayer interferometry (**Figure S1D**,**E**). It is notable that the two largest Formats, C and D, have similar hydrodynamic radii, which provided an opportunity to compare *cis* and *trans* Formats, respectively, with similar overall dimensions (**Figure S1A,E**). Formats containing scFv had greater hydrophobicity than the antibody like Format C (**Figure S1B**). Affinity was consistently 1-2 orders of magnitude higher for Her2 than CD3ε across all Formats (**Figure S1D,E**).

We next assessed the cytotoxic potency of the different TcE formats in breast cancer cell and primary activated human $CD8^+$ T-cell co-cultures. To evaluate the impact of cancer cell Her2 surface expression levels, which is a pivotal factor for TcE on-target/off-tumor targeting(30), we included two cell lines with varying Her2 membrane densities in our analysis; BT747 ductal carcinoma breast cancer cells, with high Her2 membrane density, and MCF7 mammary epithelium adenocarcinoma cells, with lower Her2 membrane density(31). We further verified and assessed expression of costimulatory ligands ICAM-1, CD58 (LFA-3) and CD80 on both cell lines by immunostaining (**Figure S2**). Cytotoxicity analysis was performed in a co-culture ratio

of 1:5 (cancer cell:T-cell) over 24 hours and assessed by LDH release assays in TcE dilution series. We found pronounced differences in cytotoxic potency between formats when assessing median effective concentrations (EC_{50}; **Figure 1C,D**). While the *cis* Formats A-C showed EC_{50} values between 3.6 and 10.0 pM for MCF7 cells and between 8.7 and 11.1 pM for BT747 cells, *trans* Format D showed significantly increased EC_{50} values of 37.6 pM and 71.2 pM for MCF7 and BT747 cells, respectively. This reduced cytotoxic potency of the *trans* Format TcE is in line with previous functional analysis of Her2/CD3ε TcEs(6). Moreover, we found increased expression of the early lymphocyte activation marker CD69 in co-cultures incubated with the *cis* TcE formats (**Figure 1E**). Similarly, regulatory cytokine receptor CD25 expression on T-cells was higher for Format A-C compared to Format D (**Figure 1F**). Release of regulatory cytokines interleukin-2 (IL-2) and tumor necrosis factor alpha (TNFα) was also increased in co-cultures treated with the *cis* Formats A-C, an effect that was most significant in low Her2 density MCF7 cells (**Figure S3**). Collectively, this indicates that the three *cis* TcEs enhanced T-cell activation similarly compared to the *trans* TcE. Based on these findings, we undertook a systematic investigation of how TcE configuration impacts potency.

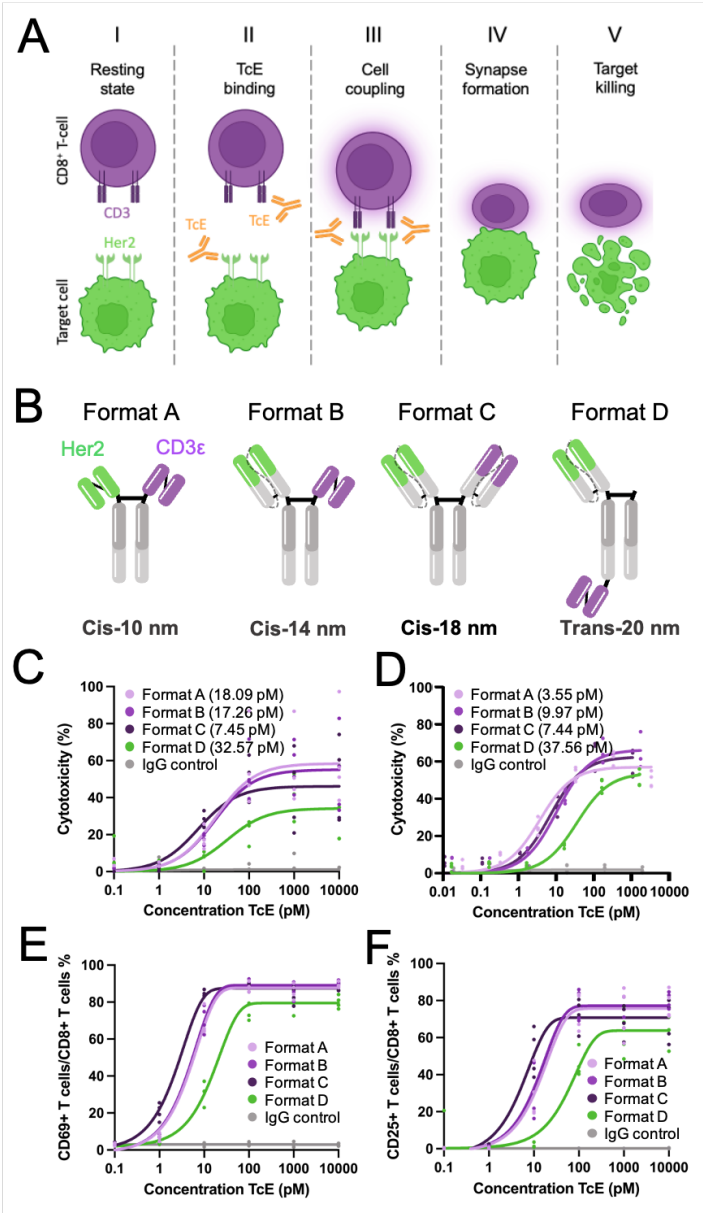

Figure 1 TcE design and functional characterization. (**A**) Schematic illustration of TcE-mediated coupling of CD3-expressing T-cells with Her2-expressing cancer cells, followed by cytolytic immune synapse formation. (**B**) Schematic illustration and paratope spacings of TcE formats tested. (**C**) and (**D**) Cytotoxicity analysis by LDH-release assessment of BT747 (C) and MCF7 (D) cells after incubation for 24 hours with primary human $CD8^+$ T-cells in a serial TcE-dilution. Values in brackets indicate EC_{50} values. (**E**) and (**F**) Flow cytometry analysis of CD69 activation marker (E) and CD25 cytokine receptor expression (F) of $CD8^+$ primary human T-cells after incubation for 24 hours with BT747 cells in a TcE serial dilution series. All experiments were performed in biological duplicates from two donors.

1

2 Initially, we assessed any potential differences in TcE-cell binding by incubation

3 of the TcE formats with human primary $CD8^+$ T-cells, MCF7 and BT747 cells and

4 subsequent staining for cell-bound TcEs with fluorescent secondary antibodies

(**Figure S4**). We found no major difference in staining intensity between TcE formats, indicating that variations in the TcE potency are not due to differences in TcE-cell binding. We further assessed whether differences in TcE potency might be attributed to discrepancies in the cell-cell coupling dynamics. For this, co-cultures of T-cells (stained with CellTracker Red) and cancer cells were incubated with TcEs and analyzed for multicellular aggregate formation by confocal microscopy **(Figure 2A)**, flow cytometry (**Figure S5**) and binding of the T-cells to cancer cell monolayers by adhesion assays (**Figure 2B,C**). T-cell-tumor cell adhesion peaked at approximately 2-4 h co-incubation but prominent TcE-format-specific differences in cell-cell coupling were not identified for either cancer cell line. Lower adhesion of T-cells in cultures treated with human serum negative control IgGs underscored that TcE-enhanced adhesion over the basal activity. The residual level of adhesion observed could be based on antigen-independent immune cell adhesion and aggregation(32, 33). Based on this, we concluded that the differences in potency between the TcE formats is not based on variations in cell-cell adhesion efficiency. However, when staining for plasma-membrane exposed luminal epitopes of CD107a (Lamp1) in these cultures, to assess T-cell degranulation, we found significantly increased staining upon addition of *cis* TcE Formats A-C (**Figure 2D,E**). This effect was most pronounced for high Her2 membrane-density BT747 cells, highlighting the role of TAA expression for TcE efficacy. Degranulation measure by CD107A is a surrogate for cytolytic protein release (e.g., granzymes and perforin) upon IS formation and a pre-requisite for $CD8^+$ T-cell killing of tumor cells(34). We therefore concluded that overall, TcE Formats A-C have similar potencies in several measures of T-cell activation, whereas Format D was distinctly weaker.

1

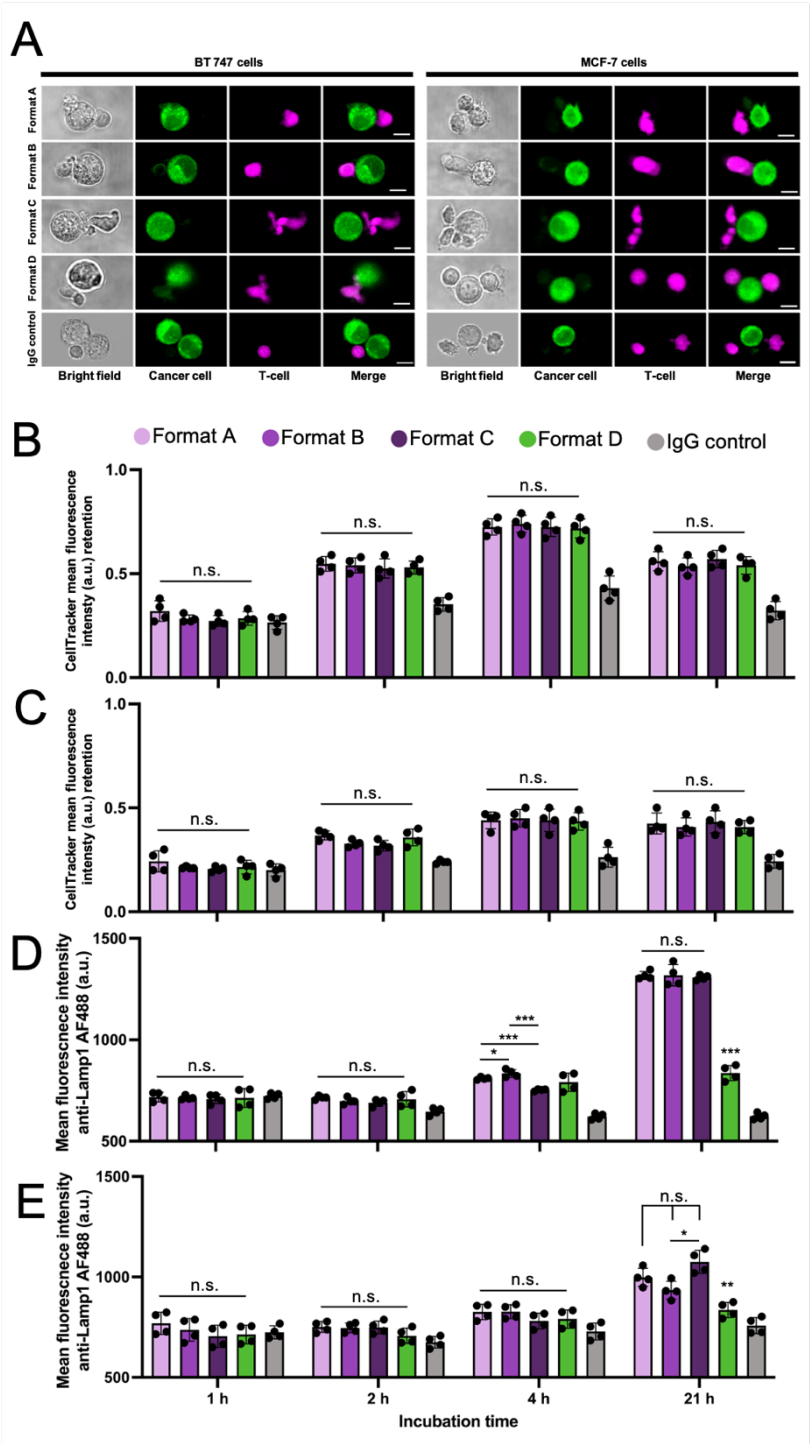

Figure 2 TcE-mediated cell coupling and induction of T-cell effector function. (**A**) Representative confocal microscopy images of Her2^{+} BT747 (left) and MCF7 (right) breast cancer lines (green) incubated with human primary CD8^{+} T-cells (magenta) for 4 hours under treatment with 5 pM TcE formats. Scale bars are 7 µm. (**B**) and (**C**) Time-resolved adhesion assays of cell coupling analysis between BT747 (B) or MCF7 (C) and human primary CD8^{+} T-cells. CellTracker-stained T-cells were incuabted on cancer cell monolayers and adhesion was quantified by fluorescence intensity analysis after washing. (**D**) and (**E**) Time-resolved flow cytometry analysis of degranulation marker (Lamp1) staining of human primary CD8^{+} T-cells incubated with BT747 (D) or MCF7 (E) and 5 pM TcEs. Experiments were performed in biological duplicates from two donors in independent experiments. One-way ANOVA with Bonferroni post-hoc testing, *p<0.05, **p<0.005, ***p<0.0005, n.s.= not significant. Statistical significance is shown as indicated by the bars or as comparasion of the treatment condition with Format D to the other formats.

Systematic analysis of immunological synapse formation

In order to perform a systematic evaluation of IS formation and extract quantitative structural parameters, we implemented a SLB system for image-based assessment by total internal reflection fluorescence microscopy (TIRF). In our system, the lipid bilayer was functionalized with fluorescently labeled and polyhistidine-tagged recombinant ICAM-1-AlexaFluor405 and Her2-AlexaFluor488 ectodomains *via* NTA(Ni^{2+}) coupling (**Figure 3A**). Based on our serial dilution EC_{50} assessment in the functional assays (see Figure 1C,D), we tested a TcE concentration of 5 pM to resolve potential differences in IS formation dynamics. To emulate the different Her2 expression levels in BT747 and MCF7 cancer cells, we applied SLB systems with either 30 (low density) or 400 (high density) Her2 ectodomain molecules/ μm^2, both presenting 200 ICAM-1 molecules/ μm^2. The time dynamics of synapse formation were resolved by fixing the cells at six time points between 5 min and 60 min post-addition to the surface, followed by staining for filamentous actin. TcE localization was imaged by staining with anti-Fc domain secondary fluorescent antibodies. A data set of over 18,000 synapse images was recorded and automated feature extraction of geometric and intensity parameters was performed.

Qualitative inspection of the data set revealed striking similarities of TcE-formed adhesion sites to IS observed in natural cell-cell and SLB systems earlier, as assessed by the interference reflection contrast signal(18, 35). Within 10 minutes post-attachment, adhesion sites with bulls-eye-like concentric actin structures, reminiscent of dSMACs, were frequently observed (**Figure 3B**). Such structures were absent in T-cell/SLBs incubated with human serum IgG controls (**Figure S6**) and in general, fewer cellular attachments to SLB were observed (1 cell per 7201 μm^2 for TcEs; 1 cell per 68304 μm^2 for IgG controls). In the center of these structures, we found accumulation

of our model TAA Her2, phenocopying the localization of TCR-pMHC in natural monofocal IS (see Figure 3B). This cSMAC-like region was also where major anti-TcE staining was detected, indicating successful TcE-based linkage of the TAA and CD3ε within the IS. We further verified this correlation by measuring colocalization of the anti-TcE signal and Her2 *via* one-to-one pixel matching (**Figure S7**). However, in contrast to mature monofocal natural IS and IS mediated by strong agonistic anti-TCR mAbs, where ICAM-1/LFA1 interactions are observed mostly with ring-like appearance in the dSMAC regions (see **Figure 3B** and **Figure S8**), we found predominantly diffusive and central accumulation of ICAM-1 in TcE-formed adhesions. Immunostaining of ICAM-1 in $CD8^+$ T-cell and cancer cell cocultures aligned with this observation, where ICAM-1 was found enriched but evenly distributed within the cell-cell contact site (**Figure S9**). Synapses with high Her2 and TcE signals were also observed for increased TcE concentration of 500 pM (100-fold increase), although adhesion sites were observed less frequently under these conditions, potentially due to saturated TcE binding of Her2 and CD3, which would suppress *trans*-synaptic binding (**Figure S10**). TcE concentrations below 0.5 pM did not elicit adhesion of the T-cells to the substrate. In addition to the monofocal configuration, we also observed a second phenotype that lacked concentric actin patterns and featured speckled puncta of Her2, anti-TcE and ICAM-1 within the cell adhesion site (**Figure S11**).

Our automated quantitative analysis revealed that high Her2 SLB densities resulted in rapid formation of large contact areas of the cells to the substrate that resulted in mature concentric synapses within the first 10 min (**Figure 3C**). This was followed by a progressive decrease in contact area over the experimental observation time. In contrast, in the case of lower Her2 SLB densities, contact area peaked between 10-15 min and progressively decrease afterwards, highlighting the impact of

TAA density on IS formation dynamics. However, we did not find any pronounced differences in contact area size measured at >15 min between the individual TcE formats. Importantly, TIRF-based assessment of the IS allowed us to simultaneously quantify the contact site topography from interference reflection contrast microscopy (IRCM) images. IRCM quantification revealed overall lower IRCM intensities for contacts formed *via* the *cis* Formats A-C compared to the Format D (**Figure 3D**). Here, lower IRCM intensities indicated closer proximity between the T-cell membrane and the SLB substrate. This was most pronounced for SLB substrates with high Her2 densities. Taken together, this demonstrates that paratope spacing of TcEs does not specifically impact on cell contact area or organization pattern during contact formation, but rather defines the membrane-membrane distance between the T cells membrane and the SLB in the IS.

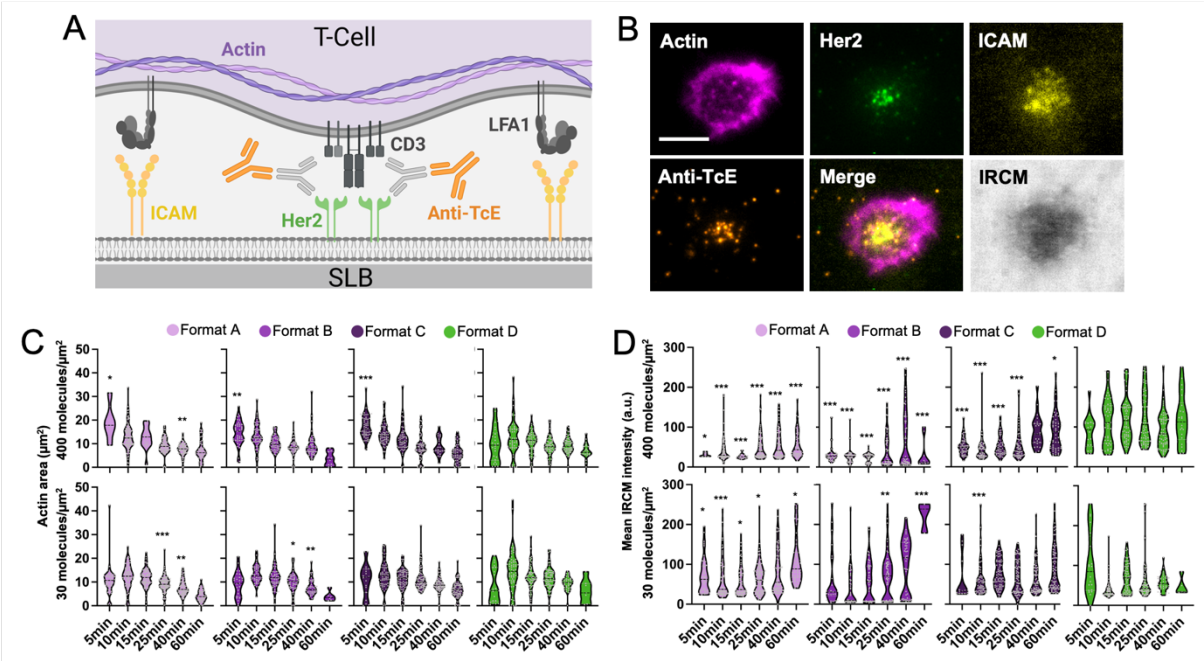

Figure 3 TcE-mediate immune synapse formation. (**A**) Schematic illustration of the SLB model system for TIRF-based analysis of immune synapse formation. (**B**) Representative TIRF images of a CD8$^+$ human primary T-cell synapse formed on a SLB system by incubation with 5 pM Format A for 25 min. Scale bar is 6 µm. (**C**) Time-resolved actin area quantification of TcE-mediated substrate adhesions formed on SLBs by CD8$^+$ human primary T-cells. Her2 densities on the SLBs are indicated on the left. (**D**) Time-resolved IRCM intensity quantification of TcE-mediated substrate adhesions formed on SLBs by CD8$^+$ human primary T-cells. Her2 densities on the SLBs are indicated on the left. Results were pooled from two donors in independent experiments. One-way ANOVA with Bonferroni post-hoc pair-wise testing in a comperasion of individual time points to the Format D condition, *$p<0.05$, **$p<0.005$, ***$p<0.0005$, n.s.= not significant. Dots indicate individual synapses and dashed lines median.

In order to resolve how this difference in membrane-membrane distance impacts on IS formation dynamics, we next quantified the formation frequency of monofocal IS-like adhesion sites over time. For this we implemented an automated detection of monofocal actin structures into our analysis pipeline *via* a global histogram-based segmentation of cell-contact areas. This was coupled to image erosion and measurement of the Hessian matrix eigenvalues of the actin staining (**Figure S12**). This allowed for automated detection of bulls-eye structures that are indicative of mature monofocal IS formation (36) as well as their discrimination against other adhesive contact sites (**Figure 4A**). We found that bull-eye structures were most frequent among contact sites between 5-15 min incubation on high Her2 density SLBs

(**Figure 4B**). In line with the previous results, this was slightly shifted towards a maximum after 10-25 min incubation on low Her2 density SLBs. Under both conditions, bulls-eye structures were mostly disassembled and cells detached from the SLBs after 60 min. Strikingly, there were large differences between the formats with *cis* and *trans* configuration. While Formats A-C formed bulls-eye structures with an average frequency of 41% of total adhesion sites over all time points, T-cells incubated with Format D only reached an average frequency of 27%. Moreover, Formats A-C showed sustained formation of IS-like adhesions over longer time periods compared to Format D, highlighting differences in the time dynamics of IS formation among the different TcE architectures. Significantly, the frequency of mature monofocal IS has been associated with the potency of immunotherapies and immune evasion in the tumor microenvironment(37, 38). Taken together, these results suggest that engager architecture regulates the time dynamics of IS formation, suggesting a mechanism for the cytotoxic potency of TcEs (see **Figure 1C, D**).

Taken together, our experiments on T-cell degranulation and IS formation frequencies show that Formats A-C are more effective in these T-cell activation measures than Format D. As our IRCM quantification also indicated that Formats A-C result in closer cell-SLB contacts than Format D, we further assessed whether this might increase the exclusion of inhibitory, large-ectodomain proteins such as CD45RABC in contact site. In order to measure this quantitatively, we added a polyhistidine-tagged fluorescent human CD45RABC-AlexaFluor647 ectodomain to our SLB system to serve as a molecular ruler. Exclusion of CD45RABC was assessed by TIRF microscopy with automated analysis of the CD45RABC fluorescence at the cell contact site within the actin ring and the surrounding SLB. In this experimental setting, we once again observed formation of adhesion sites with actin bulls-eye

structures and CD45RABC was visibly excluded from the contact, particularly in the region demarcated by the F-actin ring (**Figure 4C**). The quantification of CD45RABC intensities revealed similarly exclusion for TcE Formats A-C, whereas Format D showed significantly lower CD45RABC exclusion (**Figure 4D**). Moreover, the ratio of CD45RABC intensity in the bilayer to Her2 intensity in microclusters was lower for Formats A-C than Format D (**Figure S13A,B**). Furthermore, in a side-by-side comparison of Format C and D, in which the density of engaged Her2 was matched, we found that Format D had higher CD45RABC intensity than Format C (**Figure S13C and Figure S14**). These measurements suggest that TCR engaged by Format D is generating close contacts with an intermembrane distance ≥16 nm, a higher ratio to Her2 and higher intensity at areas of matched Her2 engagement compared to Formats A-C.

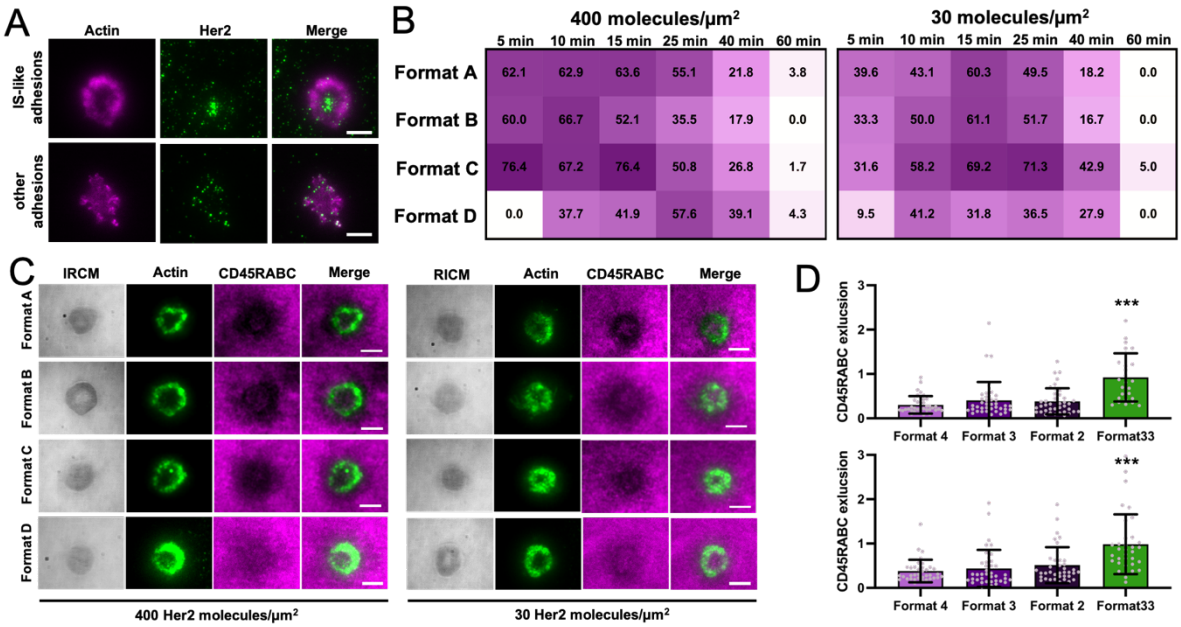

Figure 4 Size-dependent molecular reorganization at TcE-mediated immune synapses. (**A**) Representative TIRF images of immune synapse (top) and other adhesion phenotypes (bottom) formed by CD8$^+$ human primary T-cells upon incubation with 5 pM TcE formats on SLBs for 10 min. Scale bars are 7 µm. (**B**) Time resolved analysis of TcE-mediated immune synapse formation frequency of CD8$^+$ human primary T-cells on SLBs. Formats are shown on the left, Her2 densities on the SLB on top and individual values state the % of contact sites that were characterized as IS with bulls-eye actin structure. (**C**) Representative TIRF images of bulls-eye structures formed by CD8$^+$ human primary T-cells on SLBs incubated with TcEs for 25 min. SLBs additionally present 400 molecules/ µm^2 CD45RABC-AlexaFluore647 to analyze exclusion from the contact site. Her2 densities on the SLB are shown on the bottom. Scale bars are 5 µm. (**D**) Quantification of CD45RABC exclusion as shown in C for CD8$^+$ human primary T-cells incubated with 5 pM TcEs for 25 min. Each dot indicates an individual cell adhesion site plotted for the mean CD45RABC-AlexaFluor647 intensity within the actin ring divided by the mean intensity on the SLB. Shown as mean ± standard deviation with one-way ANOVA and Bonferroni post-hoc testing, ***p<0.0005. Results were pooled from two donors in independent experiments. Statistical significance is shown as comparison of the treatment condition with Format D to the other formats.

TcE-mediated inside-out T-cell signaling

Formation of cytolytic IS requires molecular self-assembly but also active patterning by T-cells that is driven by TCR-triggering and intracellular signal propagation. A key factor, among others, for establishing the cytolytic IS, and T-cell induced cytolysis, is 'inside-out' signaling, which results in increased ICAM-1 engagement(39). We therefore assessed to what extent different TcE architectures impact on active patterning *via* inside-out signaling processes by quantifying ICAM-1 recruitment in the

SLB system. We found that in each experimental condition two subpopulations with different levels of ICAM-1 recruitment, but similar IRCM signal, could be resolved (**Figure 5A**). Here, a similar IRCM signal indicates comparable substrate adhesion efficacy for both, “ICAM-1 high” and “ICAM-1 low” adhesive subpopulations. We calculated the population ratios over time for each TcE format to assess ICAM-1 recruitment (**Figure 5B**). Formats A-C produced an especially large “ICAM-1 high” population, indicative of increased integrin activation. To further evaluate if this effect is potentially driven by inside-out signaling mediated by TcE binding and IS formation, we determined if there was a linear correlation between TcE binding in the adhesion site and ICAM-1 recruitment (**Figure 5C**). The slope of this regression is indicative of the strength of the relationship between TcE-mediate cell-substrate coupling and ICAM-1 recruitment. Linear regression analysis revealed stronger positive correlations for Formats A-C compared to Format D and increasing slopes over the experimental time frame (**Figure 5D**). This suggests that these formats were particularly effective in integrin activation and ICAM-1 recruitment. In line with this, staining for intracellular signaling molecules at the IS, *i.,e.,* phospholipase Cγ (PLCγ), revealed significantly higher staining intensities for Formats A-C than Format D when using 400 Her2 molecules/μm^2, but not with 30 Her2 molecules/μm^2 (**Figure 5E**). Taken together, Formats A-C not only induced faster and more durable IS formation, but also influenced inside-out signaling pathways that further sustain IS formation and cytolysis.

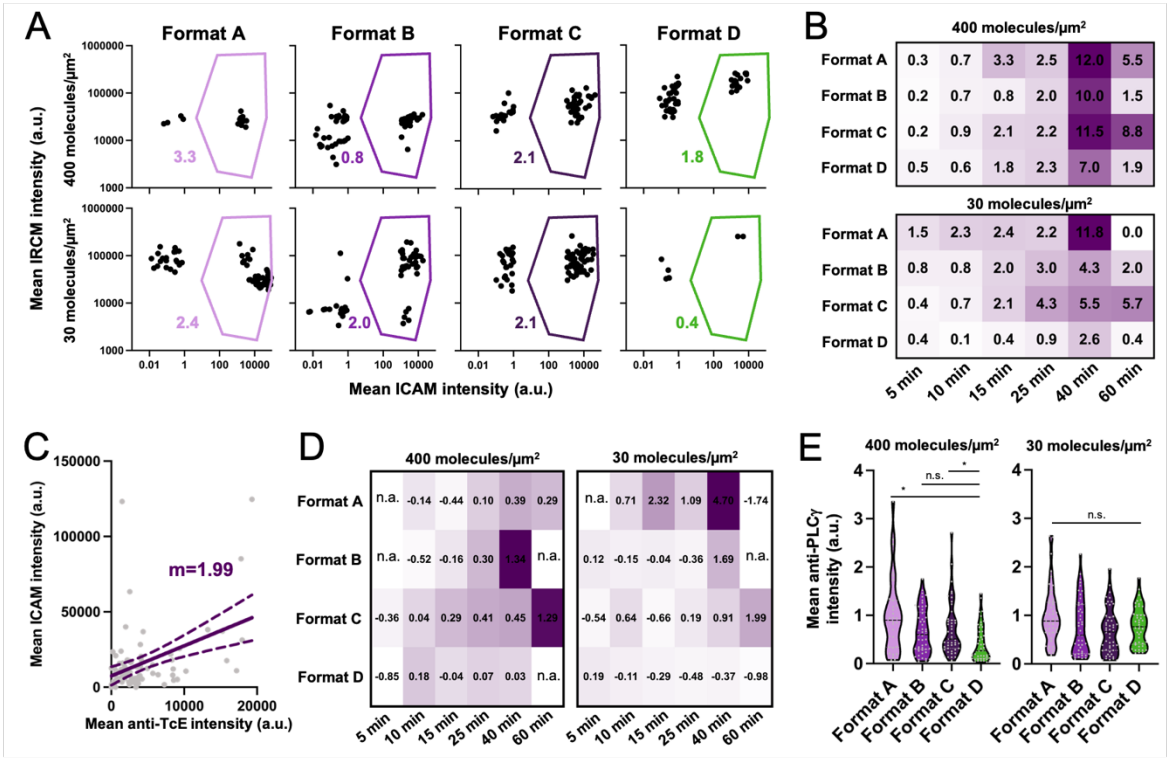

Figure 5 Analysis of TcE-regulated inside-out-signaling on SLBs. (**A**) Image cytometry analysis of differential ICAM-1 recruitment by human primary CD8$^+$ T-cells on SLBs mediated by TcEs and plotted against IRCM signal intensities. Values indicate ratio of gated (ICAM-1-high) to non-gated (ICAM-1-low) contact sites. Her2 densities on the SLB are indicated on the left and each dot shows an individual contact site. (**B**) Time resolved analysis of the ICAM1-high to ICAM-1-low population ratios of contact sites indicated in A for the four TcEs tested. Her2 densities on the SLB are indicated on top and values in the heat map indicate the population ratio for each experimental condition. (**C**) Exemplary scatter plot of mean ICAM-1 and anti Fc-PE intensities for single contact sites with linear fit from Format C at 60 min. m indicates slop of fitted curve and dashed lines the 95% confidence interval. Each dot shows an individual contact site. (**D**) Time resolved analysis of slops in linear fits as exemplified in C for the four TcE formats. Her2 densities on the SLBs are indicated on top and values in the heat map indicate the slopes for each experimental condition. N.a. = not assessed, as R^2<0.2 (**E**) Fluorescence intensity quantification of anti-PLCγ staining intensity at the IS for SLBs with 400 (left) and 30 (right) Her2 molecules/µm^2. One-way ANOVA with Bonferroni post-hoc pair-wise testing, *p<0.05, n.s.= not significant. Dots indicate individual synapses and dashed lines median. Results were pooled from two donors in independent experiments.

Discussion

Our study presents a first systematic assessment of the structure-function relationship of TcEs for immunological synapse formation. We find IgG1-based *cis* formats, using the classic IgG1 hinge were more effective than the *trans* format in which an scFv is linked at the C-terminus of the Fc. We were surprised that *cis*

configurations with two scFvs, an scFv and Fab or two Fabs had similar potency despite the differences in distance between the Her2 and CD3ε binding sites. Format D with an added Fc-linker of ~8 nm between anti-CD3 and Her2 binding arms and two hinges was comparatively less potent, but still active I killing at higher concentration. Our *in vitro* assessments demonstrate that this difference in potency is not based on variations in TcE-cell binding or cell-cell coupling efficiency but rather arises at the level of forming close contacts and inside-out signaling.

The application of reductionistic synthetic membrane models allowed us to quantify the synapse structures in high detail and throughput. However, the SLB needs to be considered as a passive molecular search system that does not fully recapitulate active processes (e.g. F-actin based restriction of mobility) and additional biophysical features (e.g. membrane topography) of the target cell. Further, while the designed SLB system does mirror Her2 densities found on target cells, it does not fully recapitulate all (co)stimulatory signals and glycocalyx components expressed on target cells. This potentially constitutes a translational limitation to the described findings but could be assessed in future experiments by addition of the respective costimulatory protein to the SLB membrane (see Figure S2). However, IS function and architecture found in SLB systems have previously been shown to be correlated with natural IS found in cell-cell interactions (40). We also found that conditions that are associated with more efficient cytotoxic function of Formats A-C compared to Format D in cellular assays, correlate well with the hierarchy of IS formation in the SLB system.

Cytolysis of target cells by lymphocytes requires TCR activation and downstream signaling for target-cell directed degranulation, which is promoted by

conformational changes, mechanotransduction, receptor clustering and exclusion of large ectodomain phosphates (e.g. CD45)(13). All the TcE formats tested here engage the TCR similarly and thus allosteric effects are likely to be similar. Mechanotransduction effects in the SLB model may be modest as the transport in SLB require very little force and directly measured forces are low(41, 42). Clustering and size exclusion effects may be reciprocally linked as failure to exclude CD45 from close contacts that can be offset by greater TCR proximity in clusters(43). Studies on size-based segregation of TCR-pMHC complexes with pMHC of varying length, revealed profound effects of adding two Ig-like domains to increase the average intermembrane spacing from 14 nm to 16 nm, suggesting that the rigid 16 nm component of the CD45 extracellular domain sets a threshold (44). Formats A-C were able to exclude CD45RABC similarly suggesting that the form close contacts of < 16 nm, while Format D didn't exclude CD45 on average suggesting that the close contacts were mostly ≥ 16 nm. These results raise two issues: First, it was surprising that Formats A-C excluded CD45 similarly as they vary significantly in size, which suggests that the close contact may be actively generated by the T cell. The *cis* TcEs may act as entropic springs to generate uniform close contacts by assuming different angles between the binding arms. The epitopes on Her2 and anti-CD3ε are both membrane proximal and its possible that using a more membrane distal TAA epitope might lead to differential potencies of Formats A-C. Second, the ability of Format D to activate partial IS formation without forming close contact < 16 nm may be due to TCR clustering at < 40 nm lateral spacing (43). The reason that Format D isn't able to accommodate close contact formation at < 16 nm despites its inherent flexibility is not clear. Its increased degrees for freedom may generate an entropic cost where the force required to position Her2 and TCR at < 16 nm is greater than can be generated

by actin-based protrusion. The resulting clusters might also be laterally disordered leading to less efficient inside out signaling and slower IS formation. We therefore conclude that the segmental flexibility of TcE is a critical structural parameter with outstanding functional importance to adapt the TAA and TCR into the “sweet spot” between clustering and phosphatase exclusion. However, adding additional degrees of freedom appears to have a cost.

Finally, it needs to be considered that cytolytic IS are transient but highly dynamic and plastic structures that require a time resolved understanding of the associated processes. Our study presents a first time-resolved analysis of TcE-mediated IS formation. We find that IS-like adhesion architectures are formed within minutes upon incubation on the substrates. The structures persist over a time period of approximately 25 min and are subsequently disassembled leading to cell detachment. Therefore, *cis* TcE-mediated IS formation mirrors the adhesion dynamics of natural, pMHC-induced IS(45). Importantly, we observed persistent slower IS formation dynamics for Format D, which correlated with lower potency in terms of both dose and maximal killing of tumour cells. However, in view of the dynamics underpinning T-cell mediated cytolysis *in vivo*, where additional factors such as TcE intratumoral diffusion, T-cell invasion and T-cell exhaustion play important roles, TcE that hit “hard and fast” are not necessarily the formats with best clinical outcome(46). Therefore, additional study will need to assess how to balance and fine-tune the cellular dynamics behind IS formation with meso- and microanatomical factors limiting the efficacy of TcE therapies.

Materials and methods

Construct design: All TcEs were constructed by recombinant DNA technology. Genes encoding variants of anti-Her2 Fabs and anti-huCD3ε were obtained by gene synthesis of light chain and heavy chain variable domains (Genewiz). Antibodies were cloned into PTT5 expression vectors for transient transfection.

The Fc region that we use for the TcEs is the human IgG1 Fc with effector function knock out (LALA) mutations. The molecules also have Genentech's knob in hole mutations in the CH3 to promote heterodimerization. The antibody does not have any other tags (like His, Myc or biotin).

Antibody expression and purification: All TcEs were expressed from transfected Chinese hamster ovary (CHO) cells. For transfection, calculated amount of different chains DNA were diluted in OptiPro SFM and sterile filtered through a 0.2 µm filter. Mirus TransIT Pro transfection reagent was added to the diluted DNA mixture and allowed to incubate for 15–30 minutes at room temperature. After the incubation period, the complex was added to the prepared CHO-E cells, and the shake flask returned to the 37° C, 5% CO_2 shaker at 200 rpm. Temperature was shifted to 30° C after 24-hour post transfection. Supernatant was harvested after 7 days by centrifuging at 4700 rpm, 4° C for 40 minutes, followed by sterile filtration through a 0.2 µm filter. Purification of the supernatant was performed in a two-step process using protein A chromatography followed by size exclusion chromatography. For this, 28 mL supernatant of each sample was loaded onto a ProPlus PhyTip (Phynexus, Catalogue#PTR 91-80-07, containing 80 µL resin) using Pyynexus MEA. The PhyTips were washed sequentially with 1.2 mL each of buffer A (DPBS, pH 6.5), buffer B (DPBS plus 1 M NaCl, pH 6.5) and buffer A again. Bound proteins were then eluted

three times, each with 0.33 mL of buffer C (30 mM NaOAc, pH 3.6). All the elution fractions were combined together and pH was adjusted using 0.01 mL of buffer D (3 M NaOAc, pH 9) with a final buffer condition as 60 mL NaOAc, pH 5. The elution fractions were further purified by size exclusion chromatography (HiLoad_26/600_Superdex_200_prep_grade). The column was first equilibrated with 600 mL of equilibration buffer (50 mM NaOAc, 100 mM NaCl, pH 5.0). Protein A elution fractions were loaded on to the column at 1.5 mL/min flow rate. Target fractions were collected and analyzed by SDS-PAGE.

Differential Scanning Calorimetry (DSC): DSC was carried out by using MicroCal VP-Capillary calorimeter (Malvern, UK) equipped with an autosampler on molecules at 1 mg/mL in (50mM acetate 100mM NaCl ph 5.0), following previously published methods(47).

Analytical Hydrophobic Interaction Chromatography (aHIC): Samples were prepared by diluting 1:1 with 2 M ammonium sulfate and analyzed using a Waters Acquity UPLC H-class system with a Sepax Proteomic HIC butyl-NP 1.7 column, 24 mg per injection. Chromatograms were generated from absorbance (l= 280 nm) detection as a function of decreasing ammonium sulfate concentration; a 16-minute elution gradient starting at 1 M ammonium sulfate, 0.1 M sodium phosphate, pH 6.5 (t=0) to 0.1 M sodium phosphate, pH 6.5 (t=16min). Data were analyzed using Empower 3 software (Waters).

Size exclusion chromatography (SEC): Analytical size exclusion chromatography was carried out using the same Agilent HPLC system. Ten micrograms of samples were

injected onto two tandemly connected Acquity BEH200 columns (Waters, 1.7 µm, 4.6 X 150 mm) at a flow rate of 0.25 mL/min. The mobile phase contains 50 mM sodium phosphate, 200 mM arginine chloride, 0.05% sodium azide, pH 6.8. The elution profile was monitored at 280 nm and manually integrated to calculate the level of high molecular weight (HMW) and low molecular weight (LMW) species.

Size exclusion chromatography-coupled multi-angular light scattering: Analytical size exclusion chromatography (SEC) in combination with multi-angular light scattering (MALS) was used to confirm the molecular weight and quality of the differently formatted antibodies. 80 µg of protein was injected through an Agilent system coupled to a light scattering detecting system (Wyatt 1422-h2 dawn heleos). The protein was separated by a TOSOH TSKgel G3000 SWxl column operated at a flow rate of 0.5 mL/min with a mobile phase of 40mM Phosphate 500mM NaCl pH 7.0. Data was analyzed by Astra software to determine the molecular weight of the main peak reported. Data was also analyzed using Empower 3 software (Waters) for the presence of high and low molecular weight species.

Dynamic light scattering: A DynaPro plate reader III (Wyatt Technology, Santa Barbara, CA) was used to carry out dynamic light scattering. Protein samples (at 1 mg/mL) were dispensed in a 384-well clear bottom plate (Aurora Microplates, Whitefish, MT). Each measurement was collected 30 times with an acquisition time of 5 sec each time at a temperature of 25 °C. Cumulant analysis was used to return intensity averaged hydrodynamic radius using DYNAMICS software (Wyatt Technology, Santa Barbara, CA).

Cell culture: Human primary $CD8^+$ cells and cancer cells (MCF-7 and BT747 obtained from the American Tissue Culture Collection, further referred to as cancer cells) were routinely cultured in RPMI (Gibco) medium supplemented with 10% fetal bovine serum, 1% penicillin/streptomycin, 1% L-glutamine, 1% non-essential amino acids and 50 mM HEPES in cell culture treated flasks at 37°C, 5% CO_2 and 100% humidity. For $CD8^+$ culture and expansion as well as for all functional assays described, 50 U/mL recombinant human IL-2 (PeproTech, UK) were added to the culture medium. Cells were split at ~80% confluency by trypsinization. Primary human $CD8^+$ were isolated from healthy donor blood with commercially available negative selection kits (RosetteSep Human $CD8^+$ T cell Enrichment Cocktail, STEMCELL technologies, UK) following the manufacturers instruction. Peripheral blood samples were provided by the National Health Service blood service under ethics agreement number 11/H711/7. After isolation, cells were expanded by addition of anti-CD3/anti-CD28 T-cell activation beads (Dynabeads ThermoFisher Scientific, UK) at 25 µL/ 10^6 cells for 3 days following the manufacturer's instructions. The magnetic beads were subsequently removed and cells were further cultured for additional 4 days without beads for expansions at 10^6 cells/mL. These cells were either used within 2 days for experiment or cryopreserved.

Surface plasmin resonance for KD: Surface plasmon resonance (SPR) was performed to analyze the binding of the TcEs to the Her2 and huCD3. The binding ability was evaluated by SPR using ProteOn XPR36, PBST-EDTA was used as the running buffer. To evaluate the binding against antigens, TcEs were captured *via* anti-Fab antibodies immobilized on the chip surfaces. Recombinant human Her2 (Sino biologicals) were run through the flow cells as analytes in a serial of concentrations.

The binding ability of each variant was evaluated by measuring the binding resonance units (RU). Binding data was processed by subtracting out the interspot binding and the buffer injections. Analysis was done using Langmire 1:1 kinetic model for Her2 binding. To evaluate the binding against huCD3, huCD3 with Fc and His tags (acquired from in-house) was immobilized to chip surface at a concentration of 0.5 ug/ mL. TcEs were diluted in the running buffer and injected into the flow cells as analytes. Analysis was done using Langmire 1:1 kinetic model.

Cell staining and immunofluorescence: Staining of cells with CellTracker Green CMFDA and CellTracker Red CMTPX (Thermo Fischer Scientific, USA) was performed at a final concentration of 5 µM for 30 min at 37°C. For quantification of surface exposure of degranulation marker Lamp-1, human primary T-cells were cocultured with cancer cells as described in the “functional assays“ section. After incubation for 1, 2, 4 and 21 hours, 100 µL of the culture medium containing T-cells were collected by aspiration. Prior to aspiration, cultures were resuspended 10 times. The cell suspension was then fixed in 4% PFA by dropwise addition for 20 min, followed by 2x washing with PBS and subsequent blocking in 1% BSA for 30 min. No permeabilization was performed. Cells were then stained with monoclonal mouse anti-human Lamp-1-AlexaFluor488 (BioLegend 328610, clone H4A3) at a final dilution of 1:500 for 1 hours. Excess antibody was removed by washing twice with 1% BSA. T-cell-specific, by pre-gating on CellTracker Red stained cells, Lamp-1 staining was quantified by flow cytometry, using a BD Fortessa X20 machine equipped with an HTS sampler.

Glass-supported lipid bilayer preparation: SLBs were prepared as described previously(48). Briefly, SLBs were generated from small unilamellar vesicles prepared by mechanical extrusion containing 12.5 mol% DOGS-NTA(Ni^{2+}) and 87.5 mol% DOPC (all lipid reagents obtained from Avanti Polar Lipids, USA) used at a final lipid concentration of 0.4 mM. Plasma-cleaned glass cover slips (SCHOTT UK Ldt, UK) were fixed to 6-lane flow chambers (sticky-Slide VI 0.4, Ibidi, Thistle Scientific LTD, UK). Each channel was filled with 80 µL of the liposome solution and incubated for 30 min at room temperature to allow for liposome attachment and fusion to the glass surface. The solution was aspirated and subsequently each channel was washed twice with flow cell buffer containing 1% BSA, 1mM $CaCl_2$, 2 mM $MgCl_2$, 10% (v/v) HEPES-buffered saline (stock concentration 200 mM HEPES pH 7.2, 1.37 M NaCl, 50 mM KCl, 5 mM Na_2HPO_4, 60 mM D-Glucose) in ddH_2O. Lipid bilayers were subsequently blocked with 3% BSA in flow cell buffer for 20 min by injecting 100 µL of the solution. Channels were washed twice with 150 µL flow cell buffer and subsequently incubated for 60 min with his-tagged recombinant human ICAM-1-AlexaFluor405 and his-tagged recombinant human Her2-AlexaFluor488 adjusted to a concentration to obtain 30 or 400 molecules/μm^2 Her2 and 200 molecules/ μm^2 ICAM-1. For CD45RABC exclusion experiments, SLBs were additionally coated with 400 molecules/μm^2 recombinant his-tagged CD45RABC-AlexaFluor647 (in this case, cells were subsequently not stained with Phalloidin-AlexaFluor647) Unbound proteins were removed by washing twice with flow cell buffer. SLBs were used within 2 hours of formation. Specific protein concentrations needed to obtain the desired molecule densities on the SLBs were deduced from calibration experiments measured by flow cytometry MFI assessment on glass bead-supported lipid bilayers. During all injection, aspiration and washing procedures, care was taken not to introduce any bubbles to

the system. For this, beads were incubated with varying amount of the recombinant his-tagged proteins and corresponding MFIs were compared to reference beads of know AlexFluor molecule densities (Bangs Laboratories, IN).

For synapse formation experiments, 150 µL of a $CD8^+$ T-cell solution was injected into the flow channels to reach a final concentration of 100.000 cells/ channel. Cells were suspended in standard cell culture medium (see above) containing 50 U/mL recombinant human IL-2. TcEs were added to the cells just prior to injection of the cell solution into the channels. After incubation, 120 µL of the solution was carefully aspirated from each channel and cells were fixed by addition of room temperature 4% PFA for 20 min. Excess PFA was removed by washing twice with 150 µL PBS, cells were permeabilized with 0.1% Tween-20 for 2 min, blocked with 1% BSA in PBS for 20 min and subsequently stained with Phalloidin-AlexaFluor647 and anti-human IgG-PE secondary antibodies, to labeled TcEs, for 1 hours. To stain for p*PLCγ*1, cells were blocked for 1h with 5% BSA in PBS and then stained with rabbit anti-p*PLCγ*1 antibody (Cell Signaling, #2821, 1/100) overnight at 4C. Samples were then washed three times with PBS and stained with goat anti-rabbit AlexaFluor Plus 405 secondary antibody (Thermofisher, A48254, 1/300) for 1h at room temperature. Excess staining solution was aspirated and samples were washed twice with 1% BSA in PBS. Imaging of the samples was performed within 7 days of sample preparation.

Confocal microscopy, TIRF imaging and image analysis: Confocal microscopy imaging was performed with a LSM880 laser scanning confocal microscope, equipped with a Plan-Apochromat, ×63, numerical aperture 1.4 oil objective. TIRFM imaging was performed with an Olympus IX83 inverted microscope (Keymed, Southend-on-Sea, UK) equipped with 405-nm, 488-nm, 561-nm and 640-nm laser lines and a

Photomertrics Evolve delta EMCCD camera. Images were acquired with a 150x 1.45 NA oil-immersion objective. If not specified otherwise, for each sample, a minimum of 30 images was recorded.

All image post-processing and analysis was performed with ImageJ (NIH). Adjustments to image brightness and contrast, as well as background corrections, were always performed on the whole image and special care was taken not to obscure or eliminate any information from the original image. For automated quantification of signal intensities, a custom-designed ImageJ macro was applied (see supplementary information). All images were first background-correct with a 50-pixel rolling ball algorithm and converted to 8-bit images. Cell attachment sites were segmented *via* intra-class variance minimization (Otsu algorithm) of the actin staining, followed by automated particle recognition and automated measurement of pixel mean or total intensities in all channels as well as particle area. For automated quantification of synapse frequencies with bulls-eye structure the actin channel for each contact site was selected and processed with a 15-pixel radius mean filter and subsequent erosion with a 10-pixel radius minimum filter. From this image, a tubbiness analysis was performed (eigenvalues of Hessian matrix), followed by segmentation of the resulting image from which bulls-eye structures were defined as those particles with pixel intensity values >0.

TcE-cell binding analysis: For analysis and quantification of TcE binding to $CD8^+$ T-cells, MFC7 and BT747 cultures, cells were trypsinized and diluted to a final concentration of 10^6 cells/ mL and washed once with PBS. Cells were then incubated with TcEs diluted in fully-supplemented culture medium (5 pM final TcE concentration) medium for 1 hour and subsequently washed twice with fully-supplemented culture

medium. Goat anti-human IgG-PE (Thermo Fischer, 12-4998-82) was then incubated with the cells at a final dilution of 1:500 for 30 min followed by washing twice with fully-supplemented culture medium and immediate imaging by confocal microscopy. Mean fluorescence intensities were calculated from maximum projection z-stacks.

Statistics and data analysis: All statistical analysis, linear regressions and plotting were performed with GraphPad Prism 9.

Functional assays: If not specified otherwise, all functional assays involving primary human $CD8^+$ T-cell/ cancer cell cocultures were performed in 96-well flat bottom transparent well plate formats (Costar 96) with a total culture volume of 150 µL and a T-cell to cancer cell ration of 1:5 with a co-incubation time of 24 hours with 50 U/mL recombinant human IL-2. Cancer cell lines were seeded on the day prior to the experiment in 100 µL fully-supplemented culture medium without recombinant human IL-2 at a concentration of 10.000 cells/well to allow adhesion. Before addition of TcEs and control IgGs, 50.000 $CD8^+$ T-cells were added in 50 µL to each culture well and subsequently TcEs were added without further delay. For time resolved functional assay, multiple technical replicates were prepared. Culture medium and cells were then collected at the indicated time points. If not stated otherwise, final TcE concentration was adjusted 500 pM.

LDH release assays (CyQuant LDH cytotoxicity assay, Thermo Fischer, USA), human IL-2 ELISA (human IL-2 Quantikine ELISA kit, R&D systems, USA) and TNFα ELISA (human TNF-alpha quantikine ELISA kit, R&D systems, USA) were performed from cell culture supernatants, following the manufacturers´ instructions.

Aggregation assay were performed to measure T-cell/cancer cell adhesion. For this, cancer cells were trypsinized from the cell culture flasks, washed with fresh cell culture medium and seeded at a concentration of 10.000 cell/well in flat bottom 96-well plates in 100 µL fully-supplemented culture medium. Primary human $CD8^+$ T-cells were immediately added to the wells afterwards at a final concentration of 50.000 cells/ well in 50 µL culture medium. Cells were incubated for time periods as indicated and subsequently removed from the well plates by aspiration. The obtained cell solution was added drop-wise to 4% PFA for fixation. Substantial unspecific aggregation of cancer cells was measured, wherefore adhesion assays were additionally performed to measure T-cell/cancer cell adhesion mediated by TcEs.

Adhesion assays were performed by seeding cancer cells at 10.000 cells/well in flat bottom transparent 96-well plates in 100 µL, followed by incubation over night to allow for cell adhesion. Subsequently, human primary T-cells, stained with CellTracker Red, were added at a concentration of 50.000 cells/well in 50 µL to the cancer cells and co-incubated for time periods as indicated. After incubation, cells were washed 3x with PBS to removed unbound and loosely-attached T-cells. Cultures were then fixed by addition of 100 µL 4% PFA, which was replaced after 20 min by PBS. Fluorescent intensities of the CellTracker Red signal in each well were then measured in each well with a FluoStar Omega microplate reader in fluorescence mode with a total number of 10 flashes in orbital averaging mode and excitation/emission filters set to 544/590 maxima (gain 2500).

ICAM-1, CD58 and CD80 immunostaining: For analysis of ICAM-1, CD58 and CD80 expression of cancer cell lines, cells were seeded in 96-well flat bottom transparent well plate formats with a total culture volume of 100 µL for 24 hours with 50 U/mL

recombinant human IL-2. Cells were subsequently washed twice with PBS and detached from the culture plates by trypsinization for 3 min. Trypsin was then blocked by addition of culture medium containing 10% FBS and cells were centrifuged at 350 rcf for 3 min. Subsequently, cells were stained with anti-human ICAM-1-AlexaFluor647 (BioXcell, BE0020-2, 3 μM), anti-human CD58-AlexaFluor647 (BD Bioscience, 563567, 1:500 dilution) or anti-human CD80-AlexaFluor647 (BioLegend, 305216, 1:500 dilution) for 30 min at room temperature in culture medium containing 1% BSA. Cultures were then washed twice with BSA-containing culture medium and fixed with 4% PFA for 20 min followed by washing twice with 1% BSA (in PBS). Stainings were analyzed by flow cytometry as described above.

For analysis of ICAM1 localization in $CD8^+$ T-cell/ cancer cell cocultures, cells were seeded and incubated as described in the “functional assays” section. Cells were seeded in 96-well flat bottom transparent well plate formats with a total culture volume of 100 μL for 4 hours with 50 U/mL recombinant human IL-2. Cells were subsequently washed twice with PBS and incubated with anti-human ICAM-1-AlexaFluor647 (BioXcell, BE0020-2, 3 μM, 1:500 dilution) for 30 min at room temperature. Cultures were then washed twice with fully-supplemented culture medium and fixed with 4% PFA for 20 min followed by washing twice with 1% BSA (in PBS). Staining was evaluated by laser-scanning confocal microscopy.

Analysis of CD45RABC exclusion form Her2 microclusters: $CD8^+$ T-cells and SLBs presenting CD45RABC were prepared as described above. From TRIF images of these samples, individual Her2 microclusters within the actin ring were manually selected at the cell attachment site. From these selections, mean fluorescence intensities for Her2 and CD45RABC were quantified by ImageJ.

Acknowledgments and funding sources: This study was supported by the Kennedy Trust for Rheumatology Research Cell Dynamics Platform and Boehringer Ingelheim Pharmaceuticals. O.S. acknowledges support from the Joachim Herz foundation (Add-on fellowship). A.L. is funded by an Erwin Schrödinger postdoctoral fellowship of the Austrian Science Fund (FWF, project number: J4542-B) and is an EMBO non-stipendiary postdoctoral fellow. We would like to thank the antibody expression and purification (APEX) team at Boehringer Ingelheim for providing high quality material to support the studies.

References

1. A. D. Waldman, J. M. Fritz, M. J. Lenardo, A guide to cancer immunotherapy: from T cell basic science to clinical practice. *Nature Reviews Immunology* **20**, 651-668 (2020).
2. A. Trabolsi, A. Arumov, J. H. Schatz, T Cell–Activating Bispecific Antibodies in Cancer Therapy. *The Journal of Immunology* **203**, 585-592 (2019).
3. U. Brinkmann, R. E. Kontermann, The making of bispecific antibodies. *MAbs* **9**, 182-212 (2017).
4. P. Roda-Navarro, L. Álvarez-Vallina, Understanding the Spatial Topology of Artificial Immunological Synapses Assembled in T Cell-Redirecting Strategies: A Major Issue in Cancer Immunotherapy. *Frontiers in cell and developmental biology* **7** (2020).
5. S. Dickopf, G. J. Georges, U. Brinkmann, Format and geometries matter: Structure-based design defines the functionality of bispecific antibodies. *Computational and Structural Biotechnology Journal* **18**, 1221-1227 (2020).
6. U. Wuellner *et al.*, Bispecific CD3/HER2 Targeting FynomAb Induces Redirected T Cell-Mediated Cytolysis with High Potency and Enhanced Tumor Selectivity. *Antibodies* **4**, 426-440 (2015).
7. J. B. Huppa, M. M. Davis, T-cell-antigen recognition and the immunological synapse. *Nature Reviews Immunology* **3**, 973-983 (2003).
8. R. Varma, G. Campi, T. Yokosuka, T. Saito, M. L. Dustin, T Cell Receptor-Proximal Signals Are Sustained in Peripheral Microclusters and Terminated in the Central Supramolecular Activation Cluster. *Immunity* **25**, 117-127 (2006).
9. W. W. A. Schamel, B. Alarcon, T. Höfer, S. Minguet, The Allostery Model of TCR Regulation. *The Journal of Immunology* **198**, 47-52 (2017).
10. Z. Reich *et al.*, Ligand-specific oligomerization of T-cell receptor molecules. *Nature* **387**, 617-620 (1997).
11. W. W. A. Schamel, B. Alarcón, Organization of the resting TCR in nanoscale oligomers. *Immunol Rev* **251**, 13-20 (2013).
12. S. T. Kim *et al.*, TCR Mechanobiology: Torques and Tunable Structures Linked to Early T Cell Signaling. *Frontiers in Immunology* **3** (2012).

13. S. J. Davis, P. A. van der Merwe, The kinetic-segregation model: TCR triggering and beyond. *Nature Immunology* **7**, 803-809 (2006).
14. S. P. Cordoba *et al.*, The large ectodomains of CD45 and CD148 regulate their segregation from and inhibition of ligated T-cell receptor. *Blood* **121**, 4295-4302 (2013).
15. A. N. R. Cartwright, J. Griggs, D. M. Davis, The immune synapse clears and excludes molecules above a size threshold. *Nature communications* **5**, 5479 (2014).
16. C. Bluemel *et al.*, Epitope distance to the target cell membrane and antigen size determine the potency of T cell-mediated lysis by BiTE antibodies specific for a large melanoma surface antigen. *Cancer Immunology, Immunotherapy* **59**, 1197-1209 (2010).
17. J. Li *et al.*, Membrane-Proximal Epitope Facilitates Efficient T Cell Synapse Formation by Anti-FcRH5/CD3 and Is a Requirement for Myeloma Cell Killing. *Cancer Cell* **31**, 383-395 (2017).
18. S. Offner, R. Hofmeister, A. Romaniuk, P. Kufer, P. A. Baeuerle, Induction of regular cytolytic T cell synapses by bispecific single-chain antibody constructs on MHC class I-negative tumor cells. *Molecular Immunology* **43**, 763-771 (2006).
19. B. H. Santich *et al.*, Interdomain spacing and spatial configuration drive the potency of IgG-[L]-scFv T cell bispecific antibodies. *Science Translational Medicine* **12**, eaax1315 (2020).
20. S. Valvo *et al.*, "Comprehensive Analysis of Immunological Synapse Phenotypes Using Supported Lipid Bilayers" in The Immune Synapse: Methods and Protocols, C. T. Baldari, M. L. Dustin, Eds. (Springer New York, New York, NY, 2017), 10.1007/978-1-4939-6881-7_26, pp. 423-441.
21. S. Venkataramani *et al.*, Design and characterization of Zweimab and Doppelmab, high affinity dual antagonistic anti-TSLP/IL13 bispecific antibodies. *Biochemical and biophysical research communications* **504**, 19-24 (2018).
22. K. Choudhuri *et al.*, Peptide-major histocompatibility complex dimensions control proximal kinase-phosphatase balance during T cell activation. *J Biol Chem* **284**, 26096-26105 (2009).
23. L. Velas *et al.*, Three-Dimensional Single Molecule Localization Microscopy Reveals the Topography of the Immunological Synapse at Isotropic Precision below 15 nm. *Nano Letters* **21**, 9247-9255 (2021).
24. X. Liu *et al.*, Human immunoglobulin G hinge regulates agonistic anti-CD40 immunostimulatory and antitumour activities through biophysical flexibility. *Nature communications* **10**, 4206 (2019).
25. K. H. Roux, L. Strelets, T. E. Michaelsen, Flexibility of human IgG subclasses. *The Journal of Immunology* **159**, 3372-3382 (1997).
26. S. Sandin, L.-G. Öfverstedt, A.-C. Wikström, Ö. Wrange, U. Skoglund, Structure and Flexibility of Individual Immunoglobulin G Molecules in Solution. *Structure (London, England : 1993)* **12**, 409-415 (2004).
27. L. R. Stingaciu, O. Ivanova, M. Ohl, R. Biehl, D. Richter, Fast antibody fragment motion: flexible linkers act as entropic spring. *Scientific reports* **6**, 22148 (2016).
28. Y. Zhang *et al.*, The Influence of Molecular Reach and Diffusivity on the Efficacy of Membrane-Confined Reactions. *Biophysical Journal* **117**, 1189-1201 (2019).
29. D. Blumenthal, J. K. Burkhardt, Multiple actin networks coordinate mechanotransduction at the immunological synapse. *Journal of Cell Biology* **219** (2020).
30. J. Middelburg *et al.*, Overcoming Challenges for CD3-Bispecific Antibody Therapy in Solid Tumors. *Cancers (Basel)* **13**, 287 (2021).

31. S. Boero *et al.*, Analysis of in vitro ADCC and clinical response to trastuzumab: possible relevance of FcγRIIIA/FcγRIIA gene polymorphisms and HER-2 expression levels on breast cancer cell lines. *Journal of Translational Medicine* **13**, 324 (2015).
32. A. Kupfer, S. J. Singer, The specific interaction of helper T cells and antigen-presenting B cells. IV. Membrane and cytoskeletal reorganizations in the bound T cell as a function of antigen dose. *J Exp Med* **170**, 1697-1713 (1989).
33. K. Somersalo *et al.*, Cytotoxic T lymphocytes form an antigen-independent ring junction. *J Clin Invest* **113**, 49-57 (2004).
34. D. T. Shen, J. S. Ma, J. Mather, S. Vukmanovic, S. Radoja, Activation of primary T lymphocytes results in lysosome development and polarized granule exocytosis in CD4+ and CD8+ subsets, whereas expression of lytic molecules confers cytotoxicity to CD8+ T cells. *J Leukoc Biol* **80**, 827-837 (2006).
35. P. F. Céspedes, D. Beckers, M. L. Dustin, E. Sezgin, Model membrane systems to reconstitute immune cell signaling. *The FEBS Journal* **n/a**.
36. Y. Kaizuka, A. D. Douglass, R. Varma, M. L. Dustin, R. D. Vale, Mechanisms for segregating T cell receptor and adhesion molecules during immunological synapse formation in Jurkat T cells. *Proceedings of the National Academy of Sciences* **104**, 20296-20301 (2007).
37. L. R. Díaz *et al.*, Imbalance of immunological synapse-kinapse states reflects tumor escape to immunity in glioblastoma. *JCI insight* **3**, e120757 (2018).
38. W. Xiong *et al.*, Immunological Synapse Predicts Effectiveness of Chimeric Antigen Receptor Cells. *Molecular Therapy* **26**, 963-975 (2018).
39. B. L. Walling, M. Kim, LFA-1 in T Cell Migration and Differentiation. *Frontiers in Immunology* **9** (2018).
40. M. L. Dustin, Supported bilayers at the vanguard of immune cell activation studies. *Journal of structural biology* **168**, 152-160 (2009).
41. P. Jönsson *et al.*, Hydrodynamic trapping of molecules in lipid bilayers. *Proceedings of the National Academy of Sciences* **109**, 10328-10333 (2012).
42. J. Göhring *et al.*, Temporal analysis of T-cell receptor-imposed forces via quantitative single molecule FRET measurements. *Nature communications* **12**, 2502 (2021).
43. H. Cai *et al.*, Full control of ligand positioning reveals spatial thresholds for T cell receptor triggering. *Nature nanotechnology* **13**, 610-617 (2018).
44. K. Choudhuri, D. Wiseman, M. H. Brown, K. Gould, P. A. van der Merwe, T-cell receptor triggering is critically dependent on the dimensions of its peptide-MHC ligand. *Nature* **436**, 578-582 (2005).
45. A. Grakoui *et al.*, The Immunological Synapse: A Molecular Machine Controlling T Cell Activation. *Science* **285**, 221-227 (1999).
46. G. Hernandez *et al.*, Pharmacodynamic Effects and Immune Correlates of Response to the CD20/CD3 Bispecific Antibody Mosunetuzumab in Relapsed or Refractory Non-Hodgkin Lymphoma. *Blood* **134**, 1585-1585 (2019).
47. S. Singh *et al.*, Selective targeting of the IL23 pathway: Generation and characterization of a novel high-affinity humanized anti-IL23A antibody. *MAbs* **7**, 778-791 (2015).
48. M. L. Dustin, T. Starr, R. Varma, V. K. Thomas, Supported planar bilayers for study of the immunological synapse. *Curr Protoc Immunol* **Chapter 18**, Unit 18.13 (2007).